Magnetic Resonance in Medicine 45:955–965 (2001)

Response of Metabolites With Coupled Spins to the STEAM Sequence

Richard B. Thompson and Peter S. Allen*

This article demonstrates that a numerical solution of the full quantum mechanical equations for all metabolites with coupled spins is an efficient and accurate means, first, of predicting the optimum STEAM sequence design for quantifying any target metabolite in brain, and, second, for providing the basis lineshapes and yields of these metabolites to facilitate their accurate quantification. Using as illustrations the weakly coupled AX_3 system of lactate, the ABX aspartyl group of N-acetylaspartate, which has only two strongly coupled spins, and the much larger strongly coupled AMNPQ glutamyl group of glutamate, the numerical solutions for the response to STEAM highlight the principal source of response variability, namely, the evolution of and transfer between zero quantum terms during the mixing time, TM. These highlights include the rapid oscillations of zero quantum terms due to the chemical shift difference of the coupled spins, the proliferation of oscillating zero order terms due to strong coupling, and the serendipitous smoothing of the response as the number of strongly coupled spins increases. The numerical solutions also demonstrate that the design of the selective 90° pulses is a far less critical factor in determining the response than was the case for the selective 180° pulses of the PRESS sequence (Thompson and Allen, Magn Reson Med 1999;41:1162–1169). The veracity of the method is demonstrated both in phantom solutions and in the parietal lobe of a normal human brain. Magn Reson Med 45: 955–965, 2001. © 2001 Wiley-Liss, Inc.

Key words: proton spectra; STEAM; coupled spins; brain

Metabolite detection and quantification in vivo with proton spectroscopic methods is most commonly carried out using the spatial localization provided either by the single voxel PRESS (point resolved spectroscopy) (1,2) or STEAM (stimulated echo acquisition mode) (3,4) sequences. When both sequences are available, the sequence of choice is often determined by the metabolite target. For example, the observation of uncoupled singlet resonances in brain, namely, N-acetylaspartate (NAA) at 2.02 ppm, creatine (Cr) at 3.05 ppm, and choline (Cho) at 3.2 ppm, are routinely observed with a long-echo PRESS sequence. This stems from the factor of two advantages in uncoupled-spin signal yield over STEAM and the relatively long T_2s of these resonances compared with either the macromolecular signals or the *J*-modulation envelopes of coupled spins. However, when the target metabolites contain coupled-spin systems, short-echo STEAM spectroscopy has gained popularity in the clinical setting, due principally to its robustness at echo times from ~10 to ~50 ms. Nonetheless, the response of certain key, coupled-spin metabolites to the STEAM sequence, not to mention the background metabolite spectrum, exhibit significant variability. The purpose of this article is to demonstrate the efficacy of numerical calculations in the determination of the sources of that variability. The range of echo and mixing times considered (TE and TM, respectively) is that which is typically regarded as falling into the short-echo experimental range, namely, TE and TM less than ~50 ms.

The short-echo-time limit is regarded as desirable for the observation of coupled spins because the longer echo-time modulations of the metabolite lineshapes lead, more often than not, to a reduction in intensity accompanied by the appearance of undesirable, oppositely phased multiplet peaks. The mitigation of transverse relaxation losses is a bonus of the shorter echo times. Nevertheless, there are limitations to the minimum sequence lengths attainable with any practical sequence. For example, finite RF pulse lengths, the time required to play out all the spoiler gradients, and the time allotted for eddy current decay all contribute to the minimum length. Moreover, unwanted contributions from broad, but short T_2, macromolecular resonances that can affect quantification are reduced if the short-echo-time limit is not pursued too vigorously. As a result of these competing factors the shorter echo-time applications of STEAM have been reported over a range of echo and mixing times between 10–50 ms.

The variability in the coupled-spin response to STEAM arises from the creation and evolution, in various parts of the sequence, of time-dependent antiphase coherences (APC) and zero quantum coherences (ZQCs), both of which influence the magnitude of components that ultimately contribute to the observable lineshape. Potentially, $N \times 2^N$ single-quantum transverse terms of the density operator evolve during the acquisition period and contribute to the lineshape of a system of N, coupled, $I = 1/2$ spins. The amplitude of each of the APC and ZQC coherence types can be significantly influenced by elements of the sequence, such as RF and gradient pulse characteristics and interpulse timings, thereby giving rise to pulse design, TE and TM dependent variations in the measured lineshape and intensity. Using numerical techniques (5) that employ the density matrix representation of nuclear spin systems, we evaluated the production and evolution of all coherence terms for several metabolite spin systems as a function of pulse design, TE and TM. This knowledge enables a TE–TM contour plot of signal intensity to be generated for any metabolite spin system or pulse envelope, so that the sequence elements can be optimized for the best yield and background discrimination. The same knowledge can also provide the prior information needed

Department of Biomedical Engineering, University of Alberta, Edmonton, Canada.

Grant sponsor: the Medical Research Council of Canada.

R.B. Thompson's current address is Laboratory of Cardiac Energetics, National Heart, Lung and Blood Institute, National Institutes of Health, Bethesda, MD 20892.

*Correspondence to: Peter S. Allen, Department of Biomedical Engineering, 1098 R.T.F., University of Alberta, Edmonton, Alberta T6G 2G3, Canada.

Received 12 June 2000; revised 13 December 2000; accepted 13 December 2000.

by nonparametric spectral fitting methods (6–8). These fitting methods employ as basis functions the appropriate full-width spectrum of each metabolite, and although these basis spectra could be obtained experimentally from a collection of individual phantoms (9), it is far more efficient to derive them numerically.

In a PRESS sequence, the coupled-spin response predicted by a hard-pulse model (reflective of manual, product-operator calculations) can differ substantially from the predictions of a full numerical solution that accommodates a selective 180° pulse design (5). In contrast to PRESS, the influence of the selective 90° pulse design of a practical STEAM sequence is not so great; it is, however, finite, particularly when higher field strengths are used (>1.5 T). With STEAM, therefore, the efficacy of numerical methods stems largely from the need to clarify the substantial effects of the coupling, rather than the need to deal with pulse design. A preliminary report of some insights from the complete numerical approach has appeared in review form (10).

The fully detailed description below first outlines the numerical methodology before highlighting the key aspects of the STEAM sequence, principally the ZQC effects in the TM period and the consequences which these effects have on the acquisition period evolution. To emphasize how these effects lead to variability in the acquired signal, a weakly coupled example, i.e., lactate (AX_3), is discussed first, comparing the complete numerical predictions with those of a previously published product operator analysis (11). Second, the strong-coupling regime is illustrated quantitatively by means of two metabolite examples that are important contributors to the 2–3 ppm region of the proton spectrum, namely, the aspartyl signal from the ABX group of NAA and the PQ and MN multiplets of the AMNPQ spin system of glutamate (Glu). Finally, the veracity of the numerical calculations is confirmed first on phantom preparations and then in vivo on normal volunteers.

NUMERICAL METHODS

When spins are not coupled their response to the STEAM sequence is well-represented by a vector model, leading to the well-known 50% yield of the sequence (3,4,12). For spins that are coupled, hard-pulse analytical models that incorporate product operator analyses of STEAM have been undertaken previously (11,13–17). However, these analyses have been confined to examples describing a small number of coupled-spins, i.e., the weakly coupled AX_3 system of lactate (11), the strongly coupled AB system of citrate (13–15), and the AB spins of the NAA aspartyl ABX group (16). In brain, many key metabolites are much more demanding, having several (e.g., five or six) strongly coupled spins and, apart from some qualitative considerations over a limited range of echo and mixing times (17), their response to STEAM has not been evaluated. To calculate this response, it is necessary to solve the Liouville-von Neumann equation (18):

$$\frac{d}{dt}\rho(t) = -i[\mathcal{H}(t), \rho(t)] \qquad [1]$$

for the time-dependent density operator of the spin system, $\rho(t)$, where $\mathcal{H}$ is the Hamiltonian under which the evolution takes place. For an N spin, I = 1/2, system the density operator $\rho(t)$ can be expressed as a weighted sum of the complete set (2^{2N}) of product operator basis terms (18), the weighting coefficients reflecting the temporal evolution of each term. The Hamiltonian used in our calculations included, in addition to the Zeeman interaction, the RF pulses, the gradient pulses, the different chemical shielding interactions, and the several scalar coupling interactions. No approximations were made for weak coupling. For time-independent Hamiltonians, Eq. [1] has a solution:

$$\rho(t) = U(t)\rho(0)U^{-1}(t) \qquad [2]$$

where $U(t) = exp(-i\,\mathcal{H}t)$. The solutions can therefore be obtained by matrix multiplication alone, if the exponential operators are expressed as matrices. When $\mathcal{H}$ corresponds to a diagonal matrix, $U(t)$ can be expressed as a diagonal matrix of exponential elements. Otherwise, $\mathcal{H}$ needs to be diagonalized by means of a unitary matrix, V, and the resulting exponential operator transformed with the same unitary matrix, so that:

$$\rho(t) = V\exp(-i\mathcal{H}_{\text{diag}}t)V^{-1}\rho(t)V\exp(i\mathcal{H}_{\text{diag}}t)V^{-1} \qquad [3]$$

where $\mathcal{H}_{diag} = V^{-1}\,\mathcal{H}\,V$, and the unitary matrix V is formed from the eigenvectors of $\mathcal{H}$. When $\mathcal{H}$ is not time-independent, for example, when shaped RF pulses are modeled, its time evolution can be subdivided into short discrete time elements, within each of which time independence of the Hamiltonian can be assumed.

In the algorithm each pulse sequence is treated as a series of independent contiguous time segments, each having its own Hamiltonian. Terms in the density operator can be evaluated at any stage during the sequence, or the acquisition period, by successive matrix multiplication according to Eq. [3]. For the gradient term in the Hamiltonian there exists a spatial distribution as well as a temporal evolution, giving rise to multiple evolution operators for each time segment or subsegment in which the gradient is applied. The gradient evolution operators for each time subsegment were collected in a storage matrix that enabled their effects to be combined efficiently irrespective of whether the ultimate FID or a midsequence density operator term was required. For selective pulses, the RF envelope was divided into 7.5 μs time subsegments and the gradient-induced frequency distribution was typically incremented to give rise to a 0.1 mm spatial resolution. Such a resolution enabled the 90% to 10% roll-off of the 90° pulse to be captured over 30–40 spatial intervals. The temporal evolution of any of the various coherences or of the ultimate transverse magnetization emerging from the sequence can easily be evaluated from the trace of the product of the density operator with the corresponding coherence or magnetization operator. Because the method of solution accommodates Hamiltonians that change relatively slowly with time, the influence of practical slice selective pulses can be calculated and contrasted with that of a hard-pulse approximation.

Table 1
Chemical Shifts, δ ppm, and Scalar Coupling Constants, *J* Hz, Used in the Calculations

Metabolite	Spin system	Chemical shifts						
		δ_A	δ_B	δ_M	δ_N	δ_P	δ_Q	δ_X
Creatine	uncoupled	3.02						
Choline	uncoupled	3.22						
NAA	uncoupled	2.023						
NAAG	uncoupled	2.05						
Lactate	AX_3	4.0908	—	—	—	—	—	1.3125
GABA	$A_2M_2X_2$	3.01	—	1.91	—	—	—	2.31
Aspartate	ABX	2.82	2.69	—	—	—	—	3.90
NAA	ABX	2.52	2.70	—	—	—	—	4.40
NAAG	ABX	2.75	2.55	—	—	—	—	4.62
NAAG	$AMNP_2$	4.15	—	1.91	2.07	2.42	—	—
Glutamate	AMNPQ	3.75	—	2.05	2.14	2.36	2.37	—
Glutamine	AMNPQ	3.76	—	2.13	2.15	2.45	2.47	—

Metabolite	Spin system	Scalar couplings											
		J_{AB}	J_{AM}	J_{AN}	J_{AX}	J_{BX}	J_{MN}	J_{MP}	J_{MQ}	J_{MX}	J_{NP}	J_{NQ}	J_{PQ}
Lactate	AX_3	—	—	—	6.933	—	—	—	—	—	—	—	—
GABA	$A_2M_2X_2$	—	7.3	—	—	—	—	—	—	7.3	—	—	—
Aspartate	ABX	17.6	—	—	4.0	8.2	—	—	—	—	—	—	—
NAA	ABX	15.5	—	—	10.1	3.7	—	—	—	—	—	—	—
NAAG	ABX	−15.9	—	—	4.37	9.5	—	—	—	—	—	—	—
NAAG	$AMNP_2$	—	8.45	4.6	—	—	−14.0	8.3	8.5	—	8.1	7.3	—
Glutamate	AMNPQ	—	7.33	4.65	—	—	−14.85	6.43	8.47	—	8.39	6.89	−15.89
Glutamine	AMNPQ	—	6.53	5.84	—	—	−14.45	6.33	9.25	—	9.16	6.35	−15.55

The chemical shielding constants and scalar coupling constants used in the numerical calculations are listed in Table 1.

STEAM SEQUENCE

Modeling of the STEAM sequence, shown in Fig. 1, requires, in addition to the RF pulses, the incorporation of three independent sets of gradients, namely, slice selection, echo, and mixing gradients. To our knowledge only two other groups have addressed such inclusions numerically (19,20). Schematically, the interpulse evolution of coherence types that are influential in causing the STEAM output variability is illustrated in Fig. 2. The first of these, arising after the first 90° pulse, is the mixture of in-phase and antiphase coherences which evolves from in-phase transverse magnetization during the first TE/2 period. The evolution is governed primarily by the scalar coupling but is also influenced by the field-strength-dependent chemical shift difference. The chemical shift (and inhomogeneous field) dephasing is ultimately recovered for the spins of the target voxel through the action of the pair of echo gradients and the second and third selective 90° pulses. The second influential coherence type is the zero quantum coherence (ZQC) group, which is generated by the second 90° pulse and which exhibits an oscillatory evolution during the mixing period, TM. The magnitude of the antiphase terms (at the end of the first TE/2) that are convertible to multiple quantum coherences by this second pulse (this includes ZQC) is governed by the choice of TE. In the subsequent TM, the mixing gradient (a filter mechanism designed to destroy all gradient sensitive magnetization) does not affect either the ZQC or the longitudinal magnetization. However, it radically dephases the transverse magnetization and higher orders of multiple quantum coherence. The evolution of ZQC during TM (to be described more fully below) determines the magnitude and character of an important set of antiphase coherence terms subsequently produced by the third 90° pulse. That set evolves to contribute to the signal during the acquisition period.

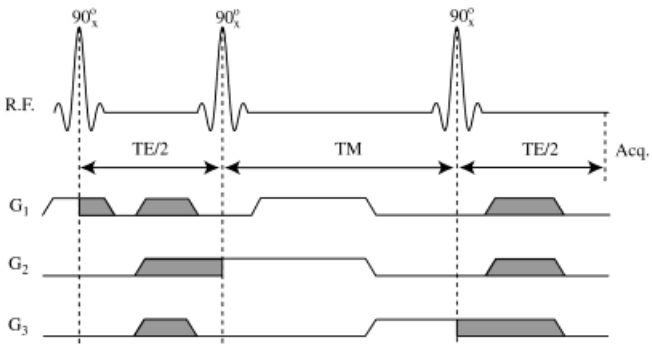

FIG. 1. An illustration of the STEAM sequence used for single voxel in vivo spectroscopy. The shaded gradients (G_i) applied prior to the midpoint of the second 90° pulse are matched by the shaded gradients following the midpoint of the third 90° pulse, refocusing both the slice and spoiler gradient evolutions. The optimized RF pulses (optsinc) have sinc envelopes optimized using the Shinnar-LaRoux procedure to give a length bandwidth product of 7.35.

RF Pulse Design Effects

It is well known that three separate mechanisms related to selective pulses serve to complicate the evolution of spins that are coupled, namely, the finite roll-off of the tip-angle

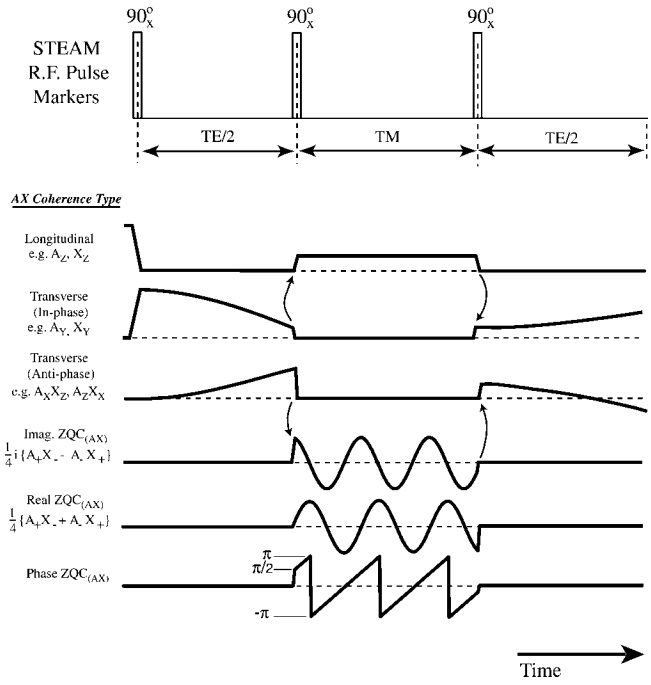

FIG. 2. A schematic illustration of the coherence evolution process which is key to the coupled-spin response to the STEAM sequence. The spoiler gradients commonly applied in both the echo and mixing periods are omitted for clarity. Following excitation, the transverse magnetization evolves (in the first TE/2 period) into a mixture of *in-phase* and *antiphase* coherence. The second 90° pulse transforms the *in-phase* coherences to longitudinal magnetization and the *antiphase* coherences to a mixture of zero quantum coherence (ZQC) and higher-order coherences. Any spoiler gradient applied during TM will dephase all coherences except the gradient-insensitive terms, namely, the longitudinal and ZQC terms. During TM, the ZQCs evolve between *real* and *imaginary* states, while the longitudinal terms are static. The final 90° pulse tips the longitudinal magnetization back to the transverse plane, but transforms only the *imaginary* part of the ZQC back to *antiphase* coherence, because of the phase-sensitivity of this process. This phase-sensitivity results in a TM-dependent production of *antiphase* coherences by the last 90° pulse. During the final TE/2 evolution period the *in-phase* and *antiphase* coherences evolve into the final mixture of transverse coherences which will determine the metabolite line shape and yield.

at the edges of the excitation band, the spatial displacement of the excitation bands of proton species that have different chemical shifts, and the continued evolution of the spins under scalar and chemically shifted Zeeman interactions during the application of the selective pulse. The consequences of these mechanisms are not entirely transparent from a hard-pulse model. First of all, they contribute to a variation in the pulse-transformed outcome for any individual coherence across the selective band of the selective pulse. However, projection operator calculations that assume hard pulses with negligible pulse width and effectively infinite bandwidth are unlikely to predict the variation in coherence transformation across the slice. To quantify this variation it is necessary to isolate the effects of RF pulse design from those of interpulse evolution. The first 90° pulse of the sequence is not a good candidate for this demonstration because only longitudinal magnetization is being transformed by it. For the remaining two pulses the isolation is not as straightforward in STEAM as was previously demonstrated in PRESS (5), where the selective 180° refocusing pulses can be treated independently of each other. In contrast to PRESS, the second and third selective 90° pulses of STEAM, together with the echo and mixing time gradients, act in concert to generate the stimulated echo. To demonstrate the difference between a selective-RF-pulse-gradient-pulse package and a hard-pulse-gradient-pulse package with the same 90° tip angles, it is necessary to reduce TM artificially in order to eliminate interpulse evolutions and hence isolate the effects of the pulses. In Fig. 3 the difference in outcome between these packages is summarized by transformation matrices. In these matrices the elements of each row reflect the weighting factors of the individual output coherences into which the RF-gradient package would convert the particular density operator component listed at the input side of the matrix (5). It should be noted that these matrix elements are only a summary, because they represent the spatially integrated effect of the pulses across their selective band. Comparing Fig. 3a and c, it is evident that both

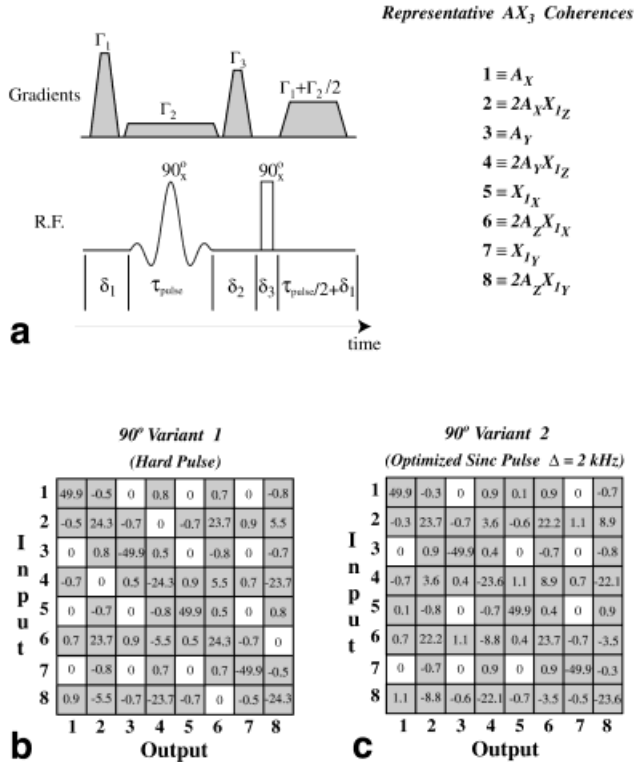

FIG. 3. To illustrate the coherence transformation properties of a realistic selective 90° pulse in comparison with an idealized, hard 90° pulse, each of these pulses is, in turn, packaged with a second, idealized hard 90° pulse, as shown in **a** for the soft pulse. The matrices delineating the transformation of eight representative lactate coherences are presented in **b** and **c**, for an idealized hard pulse and a realistic softpulse, respectively, packaged with a hard final pulse. The realistic 90° pulse had a bandwidth of 2 kHz. To ensure a valid comparison between these very different packages, δ_1 and δ_2 were set infinitesimal small and τ_{pulse} set to 3.675 ms for **c**, whereas in **b**, to keep the total sequence length identical for both cases, δ_1 and δ_2 were each set to 3.675/2 ms.

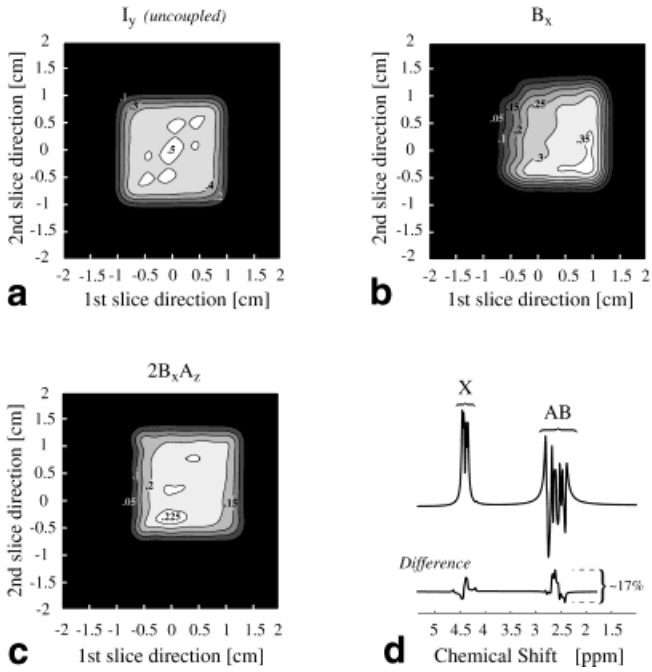

FIG. 4. A demonstration of in-slice (2nd and 3rd 90° pulses) spatial localization differences between coherences of strongly coupled spins responding to a practical STEAM sequence with TE = 30 ms and TM = 35 ms. **a:** Serving as a control, the spatial distribution of transverse magnetization, I_y, for uncoupled spins resonating at the transmitter frequency. Shallow modulations in the excitation plateau give rise to the spotty 50% level of excitation. **b:** The spatial distribution of the in-phase NAA-aspartyl term B_x. **c:** The antiphase term B_xA_z. **d:** The subsequent volume-integrated aspartyl multiplet resulting from this sequence, together with its difference from the predictions of the hard-pulse model. This difference is quantified relative to 0.5 of the uncoupled pulse-acquire signal amplitude, i.e., STEAM performance for uncoupled spins.

hard 90° pulses and practical selective 90° pulses are comparable in their ability to interchange coherences. In both cases the generation of off-diagonal elements occurs, due primarily to the coupled-spin evolutions arising from the scalar coupling and chemical shift interactions of the coupled spins. Nevertheless, there are measurable, although not substantial, differences between the distributions of alternative coherence pathways produced by the two selective pulses which can clearly be influenced by the design of the selective RF pulses.

The second principal consequence of the selective pulse design is its effect on the voxel size, shape, and location for each individual coherence term, because this also affects the ultimate metabolite yield (and lineshape). The spatial distribution of coherences produced by a slice-selective pulse is not reflected in the transformation matrix of Fig. 3, because its elements display only the spatially integrated influence of the pulse. An example of the degree of voxel degradation is illustrated in Fig. 4a–c, where examples for in-phase and antiphase coherence terms, B_x and B_xA_z, respectively, are compared with those for an uncoupled spin. The spatial distributions in Fig. 4 correspond to a point in time coincident with the start of the acquisition and result not only from the actions of the second and third pulses of the STEAM sequence (the first pulse acts only longitudinal magnetization) but also from the evolutions which occur between the pulses. The overall signal results from the action of these two pulses on an array of evolving coherences and this overall effect is illustrated in Fig. 4d, which presents the total, voxel-integrated, aspartyl coupled-spin response of NAA to a sequence with practical selective pulses, together with the difference from the predicted response of a hard-pulse model.

ZQC Effects in TM

As illustrated by Fig. 2, all except the longitudinal and ZQC terms of the density matrix are gradient-sensitive and dephased in TM by the mixing gradient. The greatest potential influence of TM on the ultimate lineshape is therefore the evolution of ZQC terms within it. In the weak-coupling limit, the TM dependence of the STEAM signal arises exclusively from the ZQC evolutions. For example, in the simplest weak-coupling example of an AX spin system the chemical shift Hamiltonian causes an oscillation between real, $1/4\{A_+X_- + A_-X_+\}$, and imaginary, $1/4i\{A_+X_- - A_-X_+\}$, components of $ZQC_{(AX)}$ at a frequency, $\delta\omega$, that is equal to the chemical shift difference between the coupled spin species. When more than two spins are involved in the weak coupling between two spin species, e.g., the AX_3 system of lactate, additional terms can evolve from a single component of $ZQC_{(AX)_1}$ due to the scalar coupling Hamiltonian. Such evolutions that occur for lactate are illustrated in Fig. 5a–c.

In contrast, if the coupling is strong, that coupling also facilitates the generation of ZQC and DQC terms directly from the longitudinal magnetization (16). Nevertheless, the largest effects do arise from ZQCs produced by the second pulse, which in this regime oscillate at a frequency that falls below $\delta\omega$, and which also, due to the strong coupling, undergo coherence transfer to ZQC terms that involve different spins. For example, in an ABX system, such as the aspartyl group of NAA, components of $ZQC_{(AX)}$ will evolve into components of $ZQC_{(BX)}$. Figure 5d–g illustrate how a single initial component, namely, the imaginary term of $ZQC_{(AX)}$, will evolve over a mixing period of 50 ms into several other zero-order terms.

Acquisition Period

Notwithstanding the fact that only in-phase transverse magnetization terms are detectable, the evolution between terms predetermines that a metabolite yield and lineshape will be governed by the distribution over antiphase, as well as in-phase, transverse coherences at the onset of the signal acquisition period. Stated mathematically, the response of an N spin, I = 1/2, system is determined by the density operator at the start of acquisition, $\sigma(TE,TM)$, which can be expressed as a weighted sum of the complete set of product operator basis terms. Of these 2^{2N} terms, there are $N \times 2^N$ that will give rise to observable magnetization, which we shall designate the T_k, together with others which do not lead to observable signals, i.e.:

$$\sigma(TE,\ TM) = \sum_{k=1}^{N2^N} a_k(TE,\ TM)T_k + \text{non-observable terms}, \quad [4]$$

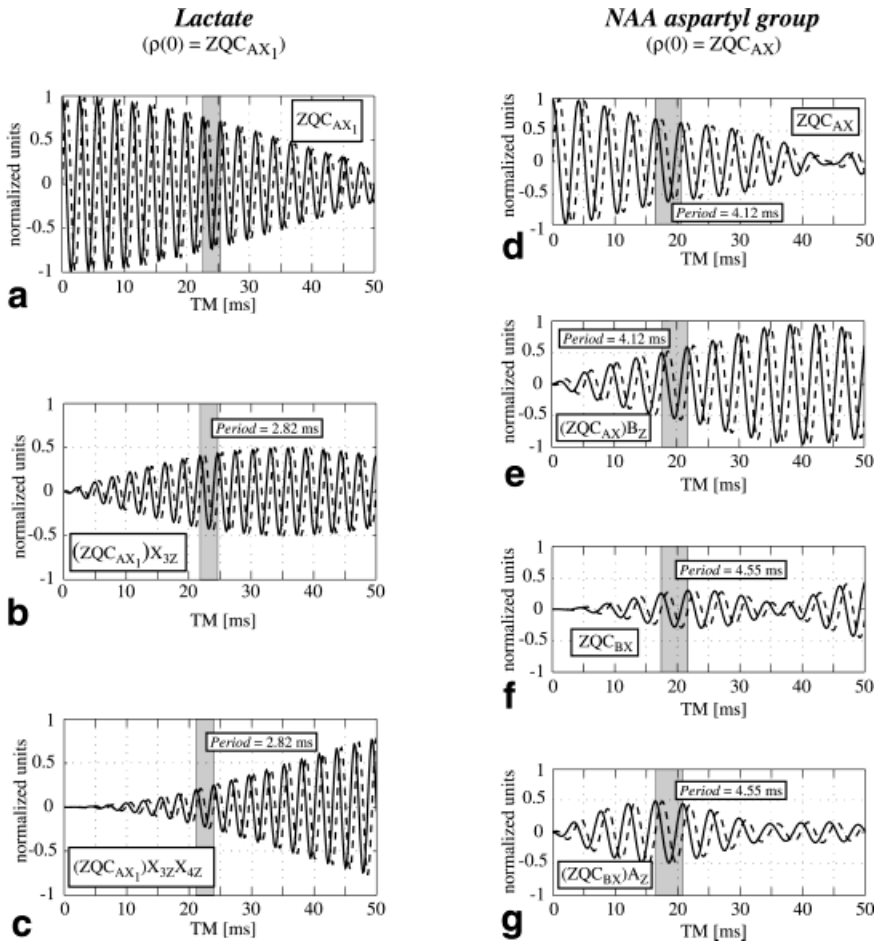

FIG. 5. An illustration of the evolution of zero-order terms in TM for both weakly and strongly coupled examples. The full lines denote imaginary components and the dashed lines the real components. The column comprising (**a,b,c**) illustrates the weakly coupled lactate case and assumes an evolution beginning with an initial state of the AX_3 system that comprises only the imaginary component of the two-spin ZQC between A and X_1, namely, $ZQC_{AX_1} = 1/4i\{A_+X_{1-} - A_-X_{1+}\} = 1/2\{A_xX_{1_y} - A_yX_{1_x}\}$. Through the scalar coupling interaction the two-spin ZQCs shown in **a** evolve to three-spin ZQCs, for example, between A, X_1 and X_3 as illustrated in **b**, as well as four-spin ZQCs, (**c**). **d–g:** Similar evolutions for the ABX spin system of NAA. The initial state illustrated again comprises a single imaginary component, namely, ZQC_{AX}. Like the AX_3 system of lactate, the two-spin ZQCs of NAA evolve into three-spin ZQCs, as shown in **e**. Unlike lactate, however, the strong coupling of the AB group results in coherence transfer, giving rise to ZQC_{BX}, as shown in **f**. The ZQC_{BX}, like ZQC_{AX}, evolves under the scalar coupling Hamiltonian to produce three-spin ZQCs as shown in **g**. In the interest of brevity, the contributions from the ZQC_{AB} terms are not displayed. The vertical gray bands delineate a single period of the ZQC oscillation.

where the weighting coefficients, a_k, are in general functions of trigonometric terms whose arguments depend on scalar coupling coefficients and chemical shifts, as well as on TE and TM. Although each of the $N \times 2^N$ single quantum (transverse) terms will evolve during acquisition, it is that evolution that produces the lineshape component that is characteristic of the originating coherence. The overall lineshape can therefore be determined from the acquisition-onset coherence distribution, as a weighted sum of the characteristic lineshape components, the weighting being governed by the magnitude of the coherence term from which the lineshape component originated. The acquisition-onset distribution of coherences itself arises from the action of the third 90° pulse followed by any preacquisition evolution during the final TE/2 period. The third 90° pulse generates in-phase coherence from the stored longitudinal magnetization and transforms certain components of the ZQCs of the coupled spins back into antiphase coherences. The magnitudes of the antiphase coherences are critically dependent on the ZQC phase evolution and the coherence transfer occurring during TM.

ILLUSTRATIONS OF SOURCES OF VARIABILITY

Lactate

In the case of the lactate doublet, for example, although the three categories of ZQC shown in Fig. 5a–c give rise, in principle, to three corresponding varieties of antiphase coherence, only one of these (A_zX_x, etc.) can evolve into observable doublet magnetization. Nevertheless, its magnitude is modified by the growth of the other two categories. Even in this simple case, the numerical approach facilitates, by means of a contour plot (Fig. 6), a clear overview of the influence of TE and TM on the intensity of the lactate doublet for a realistic localizing STEAM sequence. Cuts through the contours at specific TE or TM display a very similar oscillatory behavior to that originally calculated for such cuts using product operator techniques and assuming hard pulses (11). The numerical solution incorporating numerically optimized sinc 90° pulses (21) (bandwidth 2 kHz), gives rise to the amplitudes and frequencies shown in Fig. 6 which differ by less than 5% from the hard pulse predictions (11).

N-Acetylaspartate

For the strongly coupled NAA aspartyl ABX group, coherence transfer during TM, from $ZQC_{(AX)}$ (Fig. 5d) into $ZQC_{(BX)}$, for example (Fig. 5f), gives rise to the possibility of eight zero-order components evolving from the single imaginary $ZQC_{(AX)}$, four of which transform to antiphase coherence that can evolve into observable signal following the third 90° pulse. The other ZQC terms present at the beginning of TM will clearly give rise to many additional

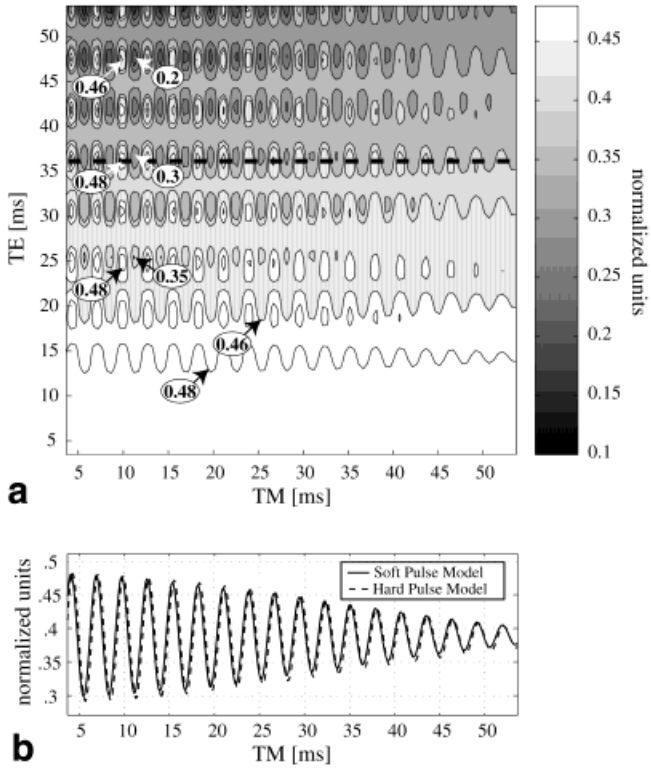

FIG. 6. **a:** A contour plot in TE-TM space of the lactate methyl doublet yield (area). **b:** A contour profile cut along a line at constant TE = 36.8 ms, emphasizing the sensitivity of the doublet area to small variations in TM. The small difference between hard pulse, product operator predictions (the dashed line), and practical selective $\pi/2$ pulses (full line) is also shown.

components at the end of TM. This proliferation of ZQC terms for strongly coupled groups of spins significantly complicates the dependence of the metabolite response to changes in TM. To illustrate this, the acquisition onset contours of two representative single-quantum transverse terms that contribute to the AB multiplet of the ABX group, centered at ~2.6 ppm, are shown in TE-TM space in Fig. 7. Contributions to each of these terms arise from several component sources. The sources are reflected in the complexity of the contour plots (Fig. 7a,d), but seen most easily in the cuts along TM shown in Fig. 7b,e. For example, the representative in-phase term B_x receives contributions from the longitudinal magnetization stored in TM (a TM-independent component), as well as the $ZQC_{(AB)}$ and $ZQC_{(BX)}$ that evolved during TM and were converted to antiphase coherence by the third 90° pulse. The relative influence of the two ZQC contributors can be gleaned from the oscillation periods, 4.12 ms for $ZQC_{(BX)}$ and 35.6 ms for $ZQC_{(AB)}$. The difference in period arises from the chemical shift difference at 3T between the coupled spins of each ZQC. The antiphase example, $2B_xX_z$, shows its $ZQC_{(BX)}$ source most clearly, oscillating in TM with a period of 4.12 ms.

Besides having a unique TE and TM dependence, each of the $N \times 2^N = 24$, transverse ABX terms in NAA also has a characteristic lineshape contribution, weighted by the acquisition-onset value of the coherence. The B_x and B_xX_z lineshape contributions are shown in Fig. 7c,f. Their magnitude in the ultimate spectrum is governed by the TM dependence shown in Fig. 7b,e. The overall lineshape and yield therefore exhibit a complex dependence on TE and TM. This is illustrated in Fig. 8a, where a map of the ~2.6 ppm peak value of the NAA aspartyl AB multiplet is displayed in TE-TM space. Because of the significant

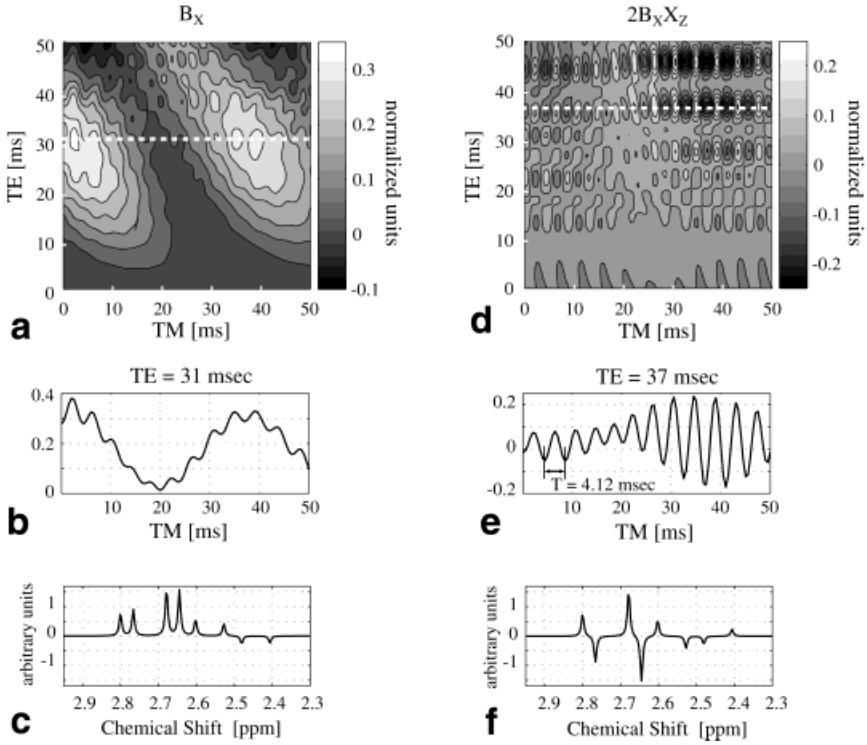

FIG. 7. The TE-TM space dependence of two representative product operator terms of the strongly coupled NAA aspartyl group at the onset of the STEAM acquisition period. The in-phase term, B_x, shown in **a–c** exhibits highly localized optimal yield (**a**), and is dominated by $ZQC_{(AB)}$ as its source, shown by the 35.6 ms period of the TE = 31 ms cut in **b**. The lineshape component associated with the B_x term is shown in **c**. The antiphase term, $2B_xX_z$, shown in **d–f** exhibits a lower yield and a more rapid variation with TM, as illustrated in **e** along the cut at TE = 37 ms, where both $ZQC_{(AX)}$ and $ZQC_{(AB)}$ oscillation frequencies are apparent. The B_xX_z lineshape component is shown in **f**.

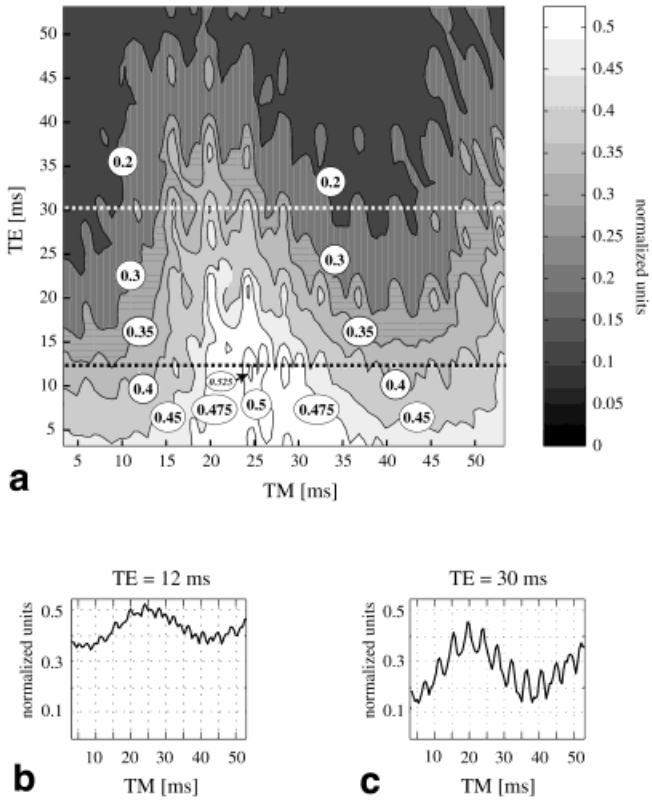

FIG. 8. The peak value of the NAA AB multiplet (at ~2.6 ppm) is shown as a contour plot in TE-TM space (**a**), and as it cuts through the contours at constant TE = 12 ms (**b**), and TE = 30 ms (**c**), emphasizing the modulation of the NAA AB yield with changes in TM. All values are normalized to the peak value of the pulse-acquire spectrum. An exponential linewidth of 5 Hz was incorporated to approximate in vivo conditions.

changes in lineshape (see Fig. 9), the spectral location of this peak value is not unique, but remains in close proximity to 2.6 ppm. The contour data were generated from the calculated spectra at intervals of 0.5 ms along each of the TE and TM axes from 0–50 ms, for a total of 10,201 spectra. The cuts shown in Fig. 8b,c along TM at constant TE demonstrate two important points that may be extended generally to all strongly coupled metabolite spins. First, both the high-frequency ($ZQC_{(AX)}$ and $ZQC_{(BX)}$) and the low-frequency ($ZQC_{(AB)}$) modulations in TM are clearly reflected in the AB multiplet yield, giving rise to a yield that is particularly sensitive to TM. Second, even at very short echo times, TE = 12 ms, the large scalar coupling between the A and B spins (15.5 Hz) results in the non-negligible production of AB antiphase coherence before the second pulse, giving rise to a significant amount of $ZQC_{(AB)}$ in TM, and to a potential reduction in yield, i.e., in this example to ~65% of the yield for uncoupled spins. At longer echo times, e.g., TE = 30 ms in Fig. 8c, the yield can be substantially suppressed relative to uncoupled spins, i.e., ~25%. The correspondence between the numerical predictions and experimental phantom spectra is shown in Fig. 9. Not only does this figure demonstrate the agreement between calculation and experiment, but it also demonstrates quite strikingly the variability of the lineshape and yield of a strongly coupled multiplet (the AB multiplet of NAA in this case) relative to the singlet acetyl resonance of NAA.

Glutamate

For the strongly coupled 5-spin AMNPQ system of Glu, there can exist as many as 220 zero-order components during TM. Relatively speaking, this makes each of the individual contributions less significant than was the case for each ZQC term of the ABX group of NAA. The outcome is therefore a smoother response in TE-TM space. For example, if we omit a term-by-term discussion in the interests of brevity and focus on the resulting spectral response, we find that at 3T (and using a 5 Hz line broadening), the dominant PQ multiplet (5,22,23) shown in Fig.

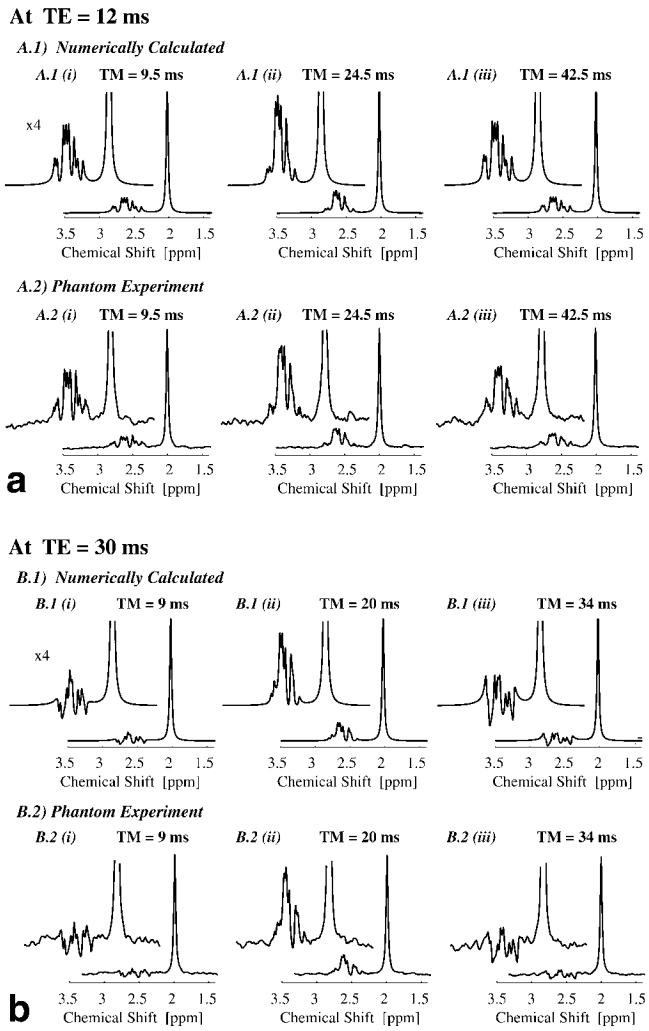

FIG. 9. A demonstration of the correspondence of calculated and experimental-phantom NAA spectra at values of TM and TE that also highlight their variability. Spectra along the TE = 12 ms cut through the contour plot of Fig. 8 are shown in A.1(i) to A.2(iii) and those along the cut at TE = 30 ms in B.1(i) to B.2(iii). Neglecting relaxation, the peak value of the NAA singlet at 2.02 ppm remains fixed at 1.0, independent of changes in TE or TM. For all spectra a linewidth of 5 Hz was incorporated to approximate in vivo conditions.

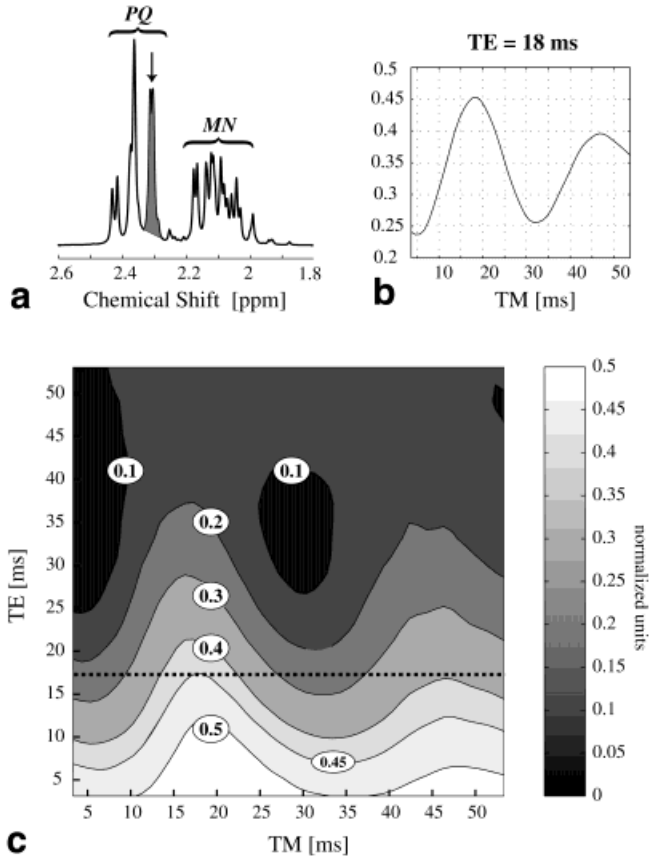

FIG. 10. An illustration of the TE-TM space dependence of the upfield component of the PQ multiplet of Glu at 2.31 ppm. **a:** The component with both shading and an arrow. **b:** Its amplitude variation as TM is varied at TE = 18 ms. **c:** The contours of this peak area in TE-TM space. The contours are normalized to the 2.31 ppm peak area from a pulse-acquire spectrum.

10a and appearing between 2.25 and 2.45 ppm, maintains a relatively stable triple-peak character. This multiplet is important in the observation of Glu in vivo because its upfield peak (arrow, Fig. 10a) falls in the gap between the corresponding PQ and MN multiplets of Gln, the principal background contaminant in vivo (see Ref. 22). The calculated area of this upfield Glu PQ peak is displayed in Fig. 10b as a cut along TM at a constant TE = 18 ms highlighting its marked TM variability, and as a TE-TM contour plot in Fig. 10c, showing the oscillations in TM and a gradual loss in intensity with TE. The TM modulation of the central PQ peaks is, however, significantly smaller than that of the upfield peak. The contour data were generated in a manner identical to that used for NAA. Both Fig. 10b and c demonstrate a characteristic evolution period of ~28 ms. This period corresponds to an effective chemical shift difference, averaged between the spins in the MN and PQ groups, of 0.266 ppm (~34 Hz at 3T) (22,23). A comparable low-frequency oscillation was observed for the yield of the NAA AB multiplet, centered at 2.6 ppm, in Fig. 8b,c. For both NAA and Glu, these low-frequency oscillations are a consequence of the relatively small chemical shift differences that exist between certain pairs of coupled spins (ω_{PQ}-ω_{MN} ~0.266 ppm, ω_B-ω_A = 0.220 ppm). Numerical and experimental phantom spectra, shown in Fig. 11, demonstrate the agreement between calculation and experiment, again highlighting the variability of the upfield PQ resonance with changes in the STEAM mixing time, TM.

IN VIVO VALIDATION

In vivo proton spectra and their computer simulations are shown in Fig. 12. The numerical spectra (Fig. 12a) were calculated for the same sequence timings, namely, TM = 20 ms and 34 ms at a TE of 30 ms as were used in the in vivo acquisition at 3.0T. The in vivo spectra arose from a $2 \times 2 \times 2$ cm^3 volume located in the parietal lobe of the brain of a healthy volunteer and are shown in Fig. 12b, where the stability of the methyl singlets of NAA (2.02 ppm), Cr (3.05 ppm), and Cho (3.24 ppm) contrasts with the significant TM sensitivity of the coupled-spin region of the spectrum (2.1 and 2.8 ppm). The offset in the ×3 enlargements is a real difference in intensity and not a displacement introduced for clarity.

In the spectral region between 2 and 3 ppm several coupled-spin metabolites contribute to the in vivo proton spectrum in addition to the strongly coupled NAA and Glu illustrated above. They include aspartate (Asp), which is similar in behavior to the aspartyl group of NAA, glutamine (Gln), whose spectral characteristics are very similar to Glu, and γ-aminobutyric acid (GABA). They also include, albeit at lower concentrations, N-acetylaspartyl glutamate (NAAG), which contains both aspartyl and glutamyl groups, as well as taurine (Tau), which contains an A_2B_2 spin system. To model the in vivo spectra, therefore, literature values for normal parietal lobe metabolite con-

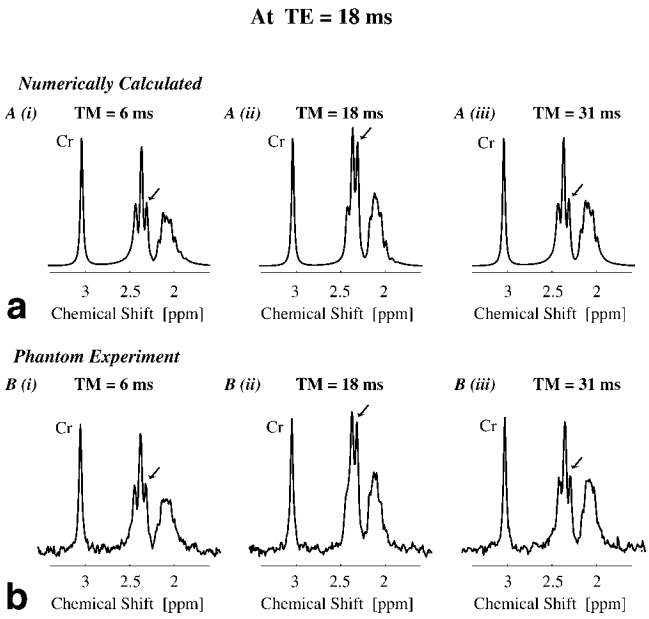

FIG. 11. A demonstration of the correspondence between calculated and experimental phantom spectra for the MNPQ multiplets of Glu, standardized relative to the 3.05 ppm singlet resonance of Cr (TE = 18 ms). The upfield component of the PQ multiplet is arrowed. The phantom solution contained 30 mM Glu together with 10 mM Cr. A 5 Hz linewidth was incorporated in all spectra to approximate in vivo conditions.

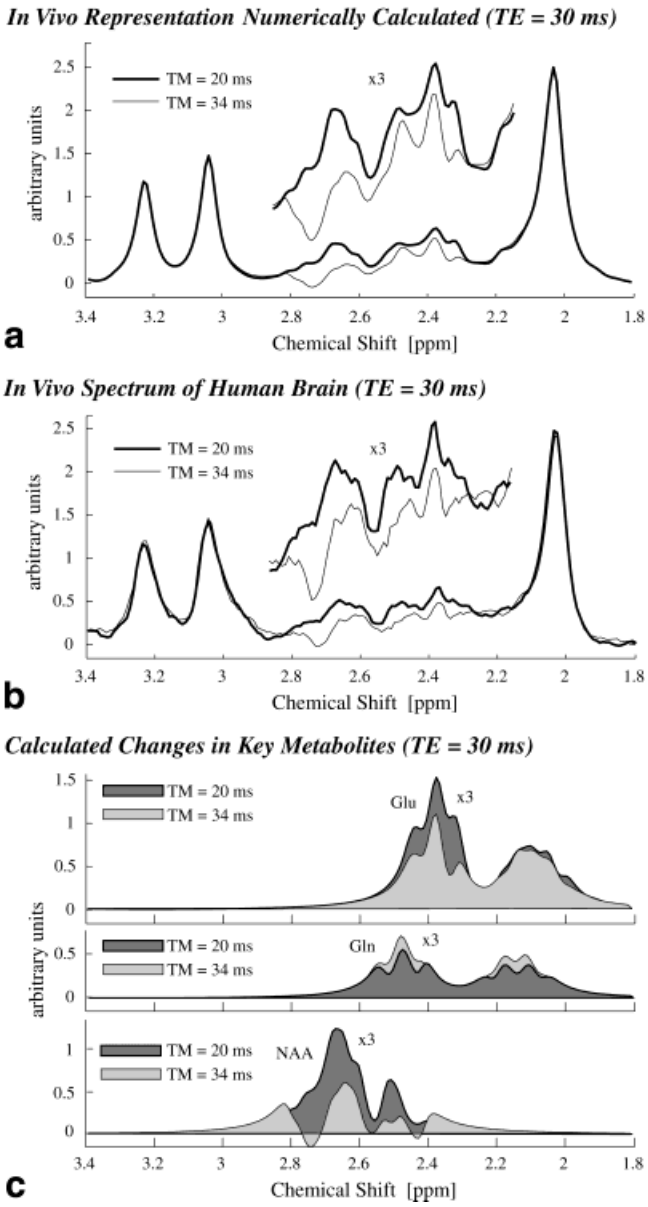

FIG. 12. A demonstration of the correspondence of the calculated (**a**) and the in vivo (**b**) spectra from human brain, as well as an in vivo demonstration of the sensitivity of coupled-spin response to the STEAM mixing time, TM. In vivo spectra were acquired at 3T from an 8 cm^3 single cubic voxel located in the parietal lobe in 256 scans with TR = 2.5 ms, and utilizing pulses and timings identical to those used in the numerical simulations. The heavier lines correspond to (TE, TM) timings of (30 ms, 20 ms), whereas the lighter lines correspond to (30 ms, 34 ms). An exponential line broadening of 1.5 Hz was applied to the in vivo data and the calculated spectra were broadened to a 7 Hz Lorentzian lineshape. The relative metabolite concentrations utilized for the calculations were (NAA : NAAG : Glu : Gln : Cr : Cho : Asp : GABA : Tau) = (8.10 : 1.60 : 7.45 : 2.65 : 6.10 : 1.39 : 1.40 : 1.40 : 1.00) from Ref. 24. The individual contributions to **a** from Glu, Gln, and NAA (AB spins) are displayed in **c**.

centrations (50% wm, 50% gm) (24) were used to determine the weighting factors of the metabolite basis spectra, in turn determined according to the Numerical Methods section (above). The consistency between in vivo and numerical spectra in the coupled-spin region not only validates the modeling but really emphasizes that if the TM variations in the lineshapes and yield are not understood, conclusions drawn about concentrations will be less than accurate. This point is highlighted further in Fig. 12c, where the individual components from the three most abundant coupled-spin groups, namely, NAA (AB resonances), Glu, and Gln, are displayed, showing that the relative intensities of any two of these metabolites are quite different at each TM across most of the overlap region.

SUMMARY AND DISCUSSION

In view of the fact that in brain the majority of proton-observable metabolites have strongly coupled spins and in view of the popularity of the short TE/TM STEAM sequence for observing such metabolites, it is essential to understand not only how this coupling might lead to inaccuracies in metabolite quantification by STEAM, but also to have a means of predicting the optimum STEAM sequence design for quantifying any particular target metabolite. The purpose of this article has been to demonstrate that a numerical solution of the quantum mechanical equations is an excellent means of dealing with each of these issues. We have shown that because the STEAM sequence uses only 90° selective pulses, the provision of alternative coherence pathways by the selective pulses is much less significant in modifying the ultimate lineshape in the STEAM case than it is in the PRESS case (5), where selective 180° pulses are used. As a result, RF pulse design differences are typically no greater than a few percent. The critical sequence-dependent spectral variability resulting from the STEAM sequence arises from the TE and TM combination. This combination governs the coherence evolution between the pulses and leads to the variety of different responses of coupled spins from that of the uncoupled singlet resonances, which are often used as standards. By means of examples which have a small number of coupled spins, namely, the weakly coupled lactate and the strongly coupled aspartyl group of NAA, we have demonstrated that even in short TE experiments significant coupled-spin evolutions can still occur and affect the yield, and that quite small changes in timings, particularly in TM, can produce marked changes in the overall lineshape and yield that are spin system- (i.e., metabolite) dependent. Although the first TE/2 period sets the stage by governing the degree to which evolution and coherence transfer enlarge the portfolio of coherences, particularly antiphase coherences immediately prior to the second 90° pulse, it is the oscillatory evolution and coherence transfer within the cohort of ZQCs that can make the ultimate lineshape so sensitive to TM. Increasing the number of coupled spins can give some relief to this sensitivity to TM. Comparison of the ABX group of NAA with the 5 spin AMNPQ spin system of Glu indicates that a greater number of coupled spins (and hence ZQC terms) tends to smear the dependency on TM. As a tool to enable one to select optimal timings for the maximization of a target metabolite and/or the minimization of a co-resonant background peak, the numerical method provides the means to express a peak-amplitude (or some other chosen measure of the

response) as a contour plot in TE-TM or any other relevant space.

The quantification of a target metabolite depends on knowing 1) the exact lineshape the target metabolite produces in response to the localizing sequence, 2) the intensity of those lineshapes relative to that of an uncoupled singlet produced by the same sequence, and 3) lineshape response of all background metabolites. Inaccuracies in metabolite quantification, or misleading comparisons between laboratories using different timing parameters, can arise if these conditions are not met. Although in principle experimental phantom spectra can provide the database of information, and although pulse design does not seem to be a significant issue with STEAM, the subtle sensitivities of the spectrum of some key metabolites to small changes in TM are not always appreciated. We propose that it is much more convenient and possibly more reliable to use a rigorous numerical approach for the planning of optimal pulse sequence timings and for the prediction of the resulting metabolite responses. Although the solutions presented here correspond exactly to a field strength of 3T, the general principles are valid at all fields. If the field is lower (1.5T), strong coupling effects are more severe, as is metabolite overlap. At higher fields the sensitivity of the coupled-spin response to small changes in TM increases due to role of chemical shift differences (in Hz) in determining the TM modulation frequencies.

ACKNOWLEDGMENTS

A studentship from the Alberta Heritage Foundation for Medical Research (to R.B.T.) is gratefully acknowledged.

REFERENCES

1. Bottomley PA. Selective volume method for performing localized NMR spectroscopy. US Patent 4,480,228, 1984.
2. Ordidge RJ, Bendall MR, Gordon RE, Connelly A. Magnetic resonance in biology and medicine. Govil G, Khetraplal CL, Saran A, editors. New Dehli: McGraw-Hill; 1985. p 387–397.
3. Frahm J, Merboldt KD, Hanicke W. Localized proton spectroscopy using stimulated echoes. J Magn Reson 1987;72:502–508.
4. Frahm J, Bruhn H, Gyngell ML, Merboldt KD, Hanicke W, Kaptein R. Localized high-resolution proton NMR spectroscopy using stimulated echoes: initial applications to human brain in vivo. Magn Reson Med 1989;9:79–93.
5. Thompson RB, Allen PS. A demonstration of the sources of variability in the response of coupled spins to the PRESS sequence and their potential impact on metabolite quantification. Magn Reson Med 1999; 41:1162–1169.
6. Soher BJ, Young K, Govindaraju V, Maudsley AA. Automated spectral analysis. III. Application to in vivo proton MR spectroscopy and spectroscopic imaging. Magn Reson Med 1998;40:822–831.
7. Young K, Soher BJ, Maudsley AA. Automated spectral analysis. II. Application of wavelet shrinkage for characterization of non-parameterized signals. Magn Reson Med 1998;40:816–821.
8. Young K, Govindaraju V, Soher BJ, Maudsley AA. Automated spectral analysis. I. Formation of a priori information by spectral simulation. Magn Reson Med 1998;40:812–815.
9. Provencher SW. Estimation of metabolite concentrations from localized in vivo proton NMR spectra. Magn Reson Med 1993;30:672–679.
10. Allen PS, Thompson RB. On the localized quantification of metabolites with coupled spins. MAGMA 1999;9:159–163.
11. Wilman AH, Allen PS. An analytical and experimental evaluation of STEAM versus PRESS for the observation of the lactate doublet. J Magn Reson 1993;B101:102–105.
12. Hahn EL. Spin echoes. Phys Rev 1950;80:580–594.
13. Wilman AH, Allen PS. The response of the strongly coupled AB system of citrate to typical 1H MRS localization sequences. J Magn Reson 1995;B107:25–33.
14. Mulkern RV, Bowers JL, Peled S, Kraft RA, Williamson DS. Citrate signal enhancement with a homonuclear J-refocusing modification to double-echo PRESS sequences. Magn Reson Med 1996;36:775–780 [erratum Magn Reson Med 1997;37:477].
15. Straubinger K, Schick F, Lutz O. Influence of pulse angle variations on stimulated echo acquisition mode proton nuclear magnetic resonance spectra of AB spin systems: theory and experiments with citrate. MAGMA 1998;7:88–94.
16. Wilman AH, Allen PS. Observing N-acetyl aspartate via both its N-acetyl and its strongly coupled aspartate groups in in-vivo proton magnetic resonance spectroscopy. J Magn Reson 1996;B113:203–213.
17. Ernst T, Hennig J. Coupling effects in volume selective 1H spectroscopy of major brain metabolites. Magn Reson Med 1991;21:82–96.
18. Ernst RR, Bodenhausen G, Wokaun A. Principles of nuclear magnetic resonance in one and two dimensions. Oxford: Clarendon Press; 1987.
19. Young K, Matson GB, Govindaraju V, Maudsley AA. Spectral simulations incorporating gradient coherence selection. J Magn Reson 1999; 140:146–152.
20. Meresi GH, Cuperlovic M, Palke WE, Gerig JT. Pulsed field gradients in simulations of one- and two-dimensional NMR spectra. J Magn Reson 1999;137:186–195.
21. Matson GB. An integrated program for amplitude-modulated RF pulse generation and re-mapping with shaped gradients. Magn Reson Imag 1994;12:1205–1225.
22. Thompson RB, Allen PS. A new multiple quantum filter design procedure for use on strongly coupled spin systems found in vivo: its application to glutamate. Magn Reson Med 1998;39:762–771.
23. Govindaraju V, Basus VJ, Matson GB, Maudsley AA. Measurement of chemical shifts and coupling constants for glutamate and glutamine. Magn Reson Med 1998;39:1011–1013.
24. Pouwels PJW, Frahm J. Regional metabolite concentrations in human brain as determined by quantitative localized proton MRS. Magn Reson Med 1998;39:53–60.